



Ultra-compact polarization rotation in integrated silicon photonics using digital metamaterials

APRATIM MAJUMDER,¹ BING SHEN,^{1,2} RANDY POLSON,³ AND RAJESH MENON^{1,*}

¹*Department of Electrical and Computer Engineering, University of Utah, Salt Lake City, UT 84112, USA*

²*Currently with Macom Inc., NY, USA*

³*Utah Nanofabrication Facility, University of Utah, Salt Lake City, UT 84112, USA*

*rmenon@eng.utah.edu

Abstract: Polarization controlling devices such as polarization splitters and rotators are critical elements in integrated-photonic circuits that function via polarization-diversity schemes. Here, we present the design of an ultra-compact nanophotonic-polarization rotator (NPR) that rotates the polarization state from TE to TM with a simulated extinction ratio of 23dB over a coupling length of 5μm and an operating bandwidth of 40nm. This all-silicon device can be fabricated in a single lithography step and we have fabricated and characterized a preliminary device exhibiting 9dB extinction ratio. To emphasize the generality of our methodology, we also designed a NPR that can rotate the polarization state from TM to TE as well. A small device footprint is enabled by the evanescent coupling of guided modes enabled by computationally designed digital metamaterials.

© 2017 Optical Society of America

OCIS codes: (350.4238) Nanophotonics and photonic crystals; (130.3120) Integrated optics devices; (160.3918) Metamaterials; (350.3950) Micro-optics.

References and links

1. V. R. Almeida, C. A. Barrios, R. R. Panepucci, and M. Lipson, "All-optical control of light on a silicon chip," *Nature* **431**(7012), 1081–1084 (2004).
2. R. Nagarajan, C. H. Joyner, R. P. Schnieder, J. S. Bostak, T. Butrie, A. G. Dentai, V. G. Dominic, P. W. Evans, M. Kato, M. Kauffman, D. J. H. Lambert, S. K. Mathis, A. Mathur, R. H. Miles, M. L. Mitchell, M. J. Missey, S. Murthy, A. C. Nilsson, F. H. Peters, S. C. Pennypacker, J. L. Pleumeekers, R. A. Salvatore, R. K. Schlenker, R. B. Taylor, M. F. Huan-Shang Tsai, V. Leeuwen, J. Webjorn, M. Ziari, D. Perkins, J. Singh, S. G. Grubb, M. S. Reffle, D. G. Mehys, F. A. Kish, and D. F. Welch, "Large-scale photonic integrated circuits," *IEEE J. Sel. Top. Quantum Electron.* **11**(1), 50–65 (2005).
3. G. T. Reed, G. Mashanovich, F. Y. Gardes, and D. J. Thomson, "Silicon optical modulators," *Nat. Photonics* **4**(8), 518–526 (2010).
4. D. Liang and J. E. Bowers, "Recent progress in lasers on silicon," *Nat. Photonics* **4**(8), 511–517 (2010).
5. C. Manolatou, S. G. Johnson, S. Fan, P. R. Villeneuve, H. A. Haus, and J. D. Joannopoulos, "High density integrated optics," *J. Lightwave Technol.* **17**(9), 1682–1692 (1999).
6. D. Dai, L. Liu, L. Wosinski, and S. He, "Design and fabrication of ultra-small overlapped AWG demultiplexer based on a Si nanowire waveguides," *Electron. Lett.* **42**(7), 400–402 (2006).
7. D. Dai, L. Liu, S. Gao, D.-X. Xu, and S. He, "Polarization management for silicon photonic integrated circuits," *Laser Photonics Rev.* **7**(3), 303–328 (2013).
8. H. Fukuda, K. Yamada, T. Tsuchizawa, T. Watanabe, H. Shinohima, and S. Itabashi, "Silicon photonic circuit with polarization diversity," *Opt. Express* **16**(7), 4872–4880 (2008).
9. T. Barwicz, M. R. Watts, M. A. Popovic, P. T. Rakich, L. Soccia, F. X. Kaertner, E. P. Ippen, and H. I. Smith, "Polarization-transparent microphotonic devices in the strong confinement limit," *Nat. Photonics* **1**(1), 57–60 (2007).
10. Y. Zhang, Y. He, J. Wu, X. Jiang, R. Liu, C. Qiu, X. Jiang, J. Yang, C. Tremblay, and Y. Su, "High-extinction-ratio silicon polarization beam splitter with tolerance to waveguide width and coupling length variations," *Opt. Express* **24**(6), 6586–6593 (2016).
11. Y. Xu, J. Xiao, and X. Sun, "Design of a compact polarization demultiplexer for silicon-based slot waveguides," *Appl. Opt.* **53**(35), 8305–8312 (2014).

12. Y. Xu and J. Xiao, "Design of a compact and integrated TM-rotated/TE-through polarization beam splitter for silicon-based slot waveguides," *Appl. Opt.* **55**(3), 611–618 (2016).
13. J. Wang, Z. Shen, and W. Wu, "Cavity-based high-efficiency and wideband 90° polarization rotator," *Appl. Phys. Lett.* **109**(15), 153504 (2016).
14. H. Fukuda, K. Yamada, T. Tsuchizawa, T. Watanabe, H. Shinohara, and S. Itabashi, "Polarization rotator based on silicon wire waveguides," *Opt. Express* **16**(4), 2628–2635 (2008).
15. M. Spanner, K. M. Davitt, and M. Y. Ivanov, "Stability of angular confinement and rotational acceleration of a diatomic molecule in an optical centrifuge," *J. Chem. Phys.* **115**(18), 8403–8410 (2001).
16. N. Kanda, T. Higuchi, H. Shimizu, K. Konishi, K. Yoshioka, and M. Kuwata-Gonokami, "The vectorial control of magnetization by light," *Nat. Commun.* **2**, 362 (2011).
17. G. D. VanWiggeren and R. Roy, "Communication with dynamically fluctuating states of light polarization," *Phys. Rev. Lett.* **88**(9), 097903 (2002).
18. V. Tsatourian, S. V. Sergeyev, C. Mou, A. Rozhin, V. Mikhailov, B. Rabin, P. S. Westbrook, and S. K. Turitsyn, "Polarisation dynamics of vector soliton molecules in mode locked fibre laser," *Sci. Rep.* **3**(1), 3154 (2013), doi:10.1038/srep03154.
19. S. V. Sergeyev, C. Mou, E. G. Turitsyna, A. Rozhin, S. K. Turitsyn, and K. Blow, "Spiral attractor created by vector solitons," *Light Sci. Appl.* **3**(1), e131 (2014), doi:10.1038/lsta.2014.12.
20. L. Liu, Y. Ding, K. Yvind, and J. M. Hvam, "Silicon-on-insulator polarization splitting and rotating device for polarization diversity circuits," *Opt. Express* **19**(13), 12646–12651 (2011).
21. Y. Ding, L. Liu, C. Peucheret, and H. Ou, "Fabrication tolerant polarization splitter and rotator based on a tapered directional coupler," *Opt. Express* **20**(18), 20021–20027 (2012).
22. H. Guan, Y. Ma, R. Shi, A. Novack, J. Tao, Q. Fang, A. E. Lim, G.-Q. Lo, T. Baehr-Jones, and M. Hochberg, "Ultracompact silicon-on-insulator polarization rotator for polarization-diversified circuits," *Opt. Lett.* **39**(16), 4703–4706 (2014).
23. C. Alonso-Ramos, R. Halir, A. Ortega-Moñux, P. Cheben, L. Vivien, I. Molina-Fernández, D. Marrs-Morini, S. Janz, D.-X. Xu, and J. Schmid, "Highly tolerant tunable waveguide polarization rotator scheme," *Opt. Lett.* **37**(17), 3534–3536 (2012).
24. Y. Zhang, Y. He, X. Jiang, B. Liu, C. Qiu, Y. Su, and R. A. Soref, "Ultra-compact and highly efficient silicon polarization splitter and rotator," *APL Photonics* **1**(9), 091304 (2016).
25. L. Gao, Y. Huo, J. S. Harris, and Z. Zhou, "Ultra-compact and low-loss polarization rotator based on asymmetric hybrid plasmonic waveguide," *IEEE Photonics Technol. Lett.* **25**(21), 2081–2084 (2013).
26. J. Zhang, S. Zhu, H. Zhang, S. Chen, G.-Q. Lo, and D.-L. Kwong, "An ultracompact surface plasmon polariton-effect-based polarization rotator," *IEEE Photonics Technol. Lett.* **23**(21), 1606–1608 (2011).
27. R. R. Andrawis, M. A. Swillam, and E. A. Soliman, "Submicron omega-shaped plasmonic polarization rotator," *J. Opt.* **16**(10), 105001 (2014).
28. J. N. Caspers, J. S. Aitchison, and M. Mojahedi, "Experimental demonstration of an integrated hybrid plasmonic polarization rotator," *Opt. Lett.* **38**(20), 4054–4057 (2013).
29. M. F. Hameed and S. S. Obayya, "Design of passive polarization rotator based on silica photonic crystal fiber," *Opt. Lett.* **36**(16), 3133–3135 (2011).
30. L. Lu, L. L. Cheong, H. I. Smith, S. G. Johnson, J. D. Joannopoulos, and M. Soljačić, "Three-dimensional photonic crystals by large-area membrane stacking," *Opt. Lett.* **37**(22), 4726–4728 (2012).
31. C. J. Kirby, P. Chang, A. S. Helmy, and A. Y. Elezzabi, "Magnetoplasmonic Faraday rotators: Enabling gigahertz active polarization control for integrated plasmonics," *ACS Photonics* **3**(12), 2344–2352 (2016).
32. B. Shen, P. Wang, R. C. Polson, and R. Menon, "An integrated-nanophotonics polarization beamsplitter with $2.4 \times 2.4 \mu\text{m}^2$ footprint," *Nat. Photonics* **9**(6), 378–382 (2015).
33. B. Shen, R. Polson, and R. Menon, "Increasing the density of passive photonic-integrated circuits via nanophotonic cloaking," *Nat. Commun.* **7**, 13126 (2016), doi:10.1038/ncomms13126.
34. B. Shen, P. Wang, R. Polson, and R. Menon, "Integrated metamaterials for efficient and compact free-space-to-waveguide coupling," *Opt. Express* **22**(22), 27175–27182 (2014).
35. B. Shen, R. Polson, and R. Menon, "Metamaterial-waveguide bends with effective bend radius $\lambda_0/2$," *Opt. Lett.* **40**(24), 5750–5753 (2015).
36. B. Shen, R. Polson, R. Menon, and R. Menon, "Integrated digital metamaterials enables ultra-compact optical diodes," *Opt. Express* **23**(8), 10847–10855 (2015).
37. J. Lu and J. Vučković, "Nanophotonic computational design," *Opt. Express* **21**(11), 13351–13367 (2013).
38. A. Y. Piggott, J. Lu, K. G. Lougadakis, J. Petykiewicz, T. M. Babinec, and J. Vuckovic, "Inverse design and demonstration of a compact and broadband on-chip wavelength demultiplexer," *Nat. Photonics* **9**(6), 374–377 (2015).
39. G. Kim, J.-A. Dominguez-Caballero, H. Lee, D. J. Friedman, and R. Menon, "Increased photovoltaic power output via diffractive spectrum separation," *Phys. Rev. Lett.* **110**(12), 123901 (2013).
40. M. A. Seldowitz, J. P. Allebach, and D. W. Sweeney, "Synthesis of digital holograms by direct binary search," *Appl. Opt.* **26**(14), 2788–2798 (1987).
41. M. R. Black, "Losses in polysilicon waveguides," Thesis (M. Eng.), Massachusetts Institute of Technology, Dept. of Electrical Engineering and Computer Science (1995).

42. C. Lehrer, L. Frey, S. Petersen, M. Mizutani, M. Takai, and H. Ryssel, "Defects and gallium-contamination during focused ion beam micro machining," International Conference on Ion Implantation Technology, 695–698, (2000).
43. R. Menon, P. Rogge, and H.-Y. Tsai, "Design of diffractive lenses that generate optical nulls without phase singularities," J. Opt. Soc. Am. A **26**(2), 297–304 (2009).

1. Introduction

Recently, photonic-integrated circuits (PICs) fabricated on the silicon-on-insulator (SOI) platform have generated substantial interest due to low power consumption, high efficiency, small footprint and compatibility with complementary metal-oxide-semiconductor (CMOS) fabrication processes [1–4]. The SOI platform has remained the popular choice in this field due to the high refractive index contrast that exists between silicon and silicon dioxide. However, this property results in birefringence that causes silicon-photonics devices to be highly polarization dependent [5, 6]. One solution is to employ devices and photonic circuits that function via polarization-diversity schemes [7–9]. The critical elements in such circuits are polarization splitters [10–12] and polarization rotators [13–14]. Other applications of polarization control include but are not limited to trapping and manipulation of atoms and nanoparticles [15], control of magnetization [16], optical communication [17], development of mode locked fiber lasers [18,19], etc. One way of achieving polarization rotation is to use the cross-polarization coupling effect [20]. This device achieved an extinction ratio of 12dB with -0.06dB insertion loss over a coupling length of $36.8\mu\text{m}$. A related device is a polarization splitter and rotator that is tolerant to fabrication errors based on a tapered directional coupler [21]. However, these devices require coupling lengths in the range of $100\mu\text{m}$ to $200\mu\text{m}$. A smaller polarization rotator with a length of $15.3\mu\text{m}$ and extinction ratio $>25\text{dB}$ and another design based on the excitation of two hybrid modes, achieving $>40\text{dB}$ extinction ratio have also been reported [22, 23]. However, neither of the devices have been experimentally demonstrated. A polarization splitter and rotator with coupling length of $8.77\mu\text{m}$ that utilizes TM cross-polarization coupling between two parallel and bent silicon waveguides has also been reported [24]. In this device, the waveguide radii are carefully optimized to achieve the best cross-polarization coupling and selection of the desired modes. However, the device area as measured from the input port to the output port is about $15.7\mu\text{m} \times 7.8\mu\text{m} = 105\mu\text{m}^2$. Nevertheless, the device performance is excellent, exhibiting high conversion efficiencies and low loss. However, in this device polarization splitting and rotation are interlinked phenomena, thereby always rotating the cross-coupled TM mode to TE at the output. Therefore, this device would not allow for a separate TM polarized output. A different class of polarization rotators have also been demonstrated that exploit surface-plasmon polariton (SPP) resonances [25–28], of which the smallest device in terms of simulations has coupling length less than $1\mu\text{m}$ [27], while the smallest experimentally demonstrated device has coupling length of about $3\mu\text{m}$ [28]. However, these devices suffer from high loss, rotational asymmetry and fabrication complexity due to introduction of gold. The latter also makes these devices incompatible with standard CMOS processes. Photonic-crystal-based polarization controllers in silicon have also been demonstrated [29, 30]. Recently, a new design of an integrated magneto-plasmonic Faraday rotator that is predicted to achieve 99.4% polarization conversion over an $830\mu\text{m}$ coupling length has also been proposed [31]. However, that device has not been experimentally demonstrated yet.

Here, we designed, fabricated and characterized a nanophotonic-polarization rotator (NPR) based on the concept of computationally designed 'digital metamaterials'. Our device is comprised of only silicon, is CMOS compatible, occupies an area of $5\mu\text{m} \times 1.2\mu\text{m}$, and can be fabricated with a single lithography step. Previously, digital metamaterials have been used to create various ultra-compact devices including polarization beamsplitters [32], densely packed waveguides [33], free-space-to-waveguide couplers [34–36], and wavelength splitters [37,38]. In general, we use a computationally driven design to engineer the refractive index of a region of silicon at the sub-wavelength scale to achieve a specific photonic function. In this

case, the function is polarization rotation in a waveguide. It is to be noted that these devices operate via the coupling among a number of resonant nanophotonic modes and thus not only exhibit a small footprint, but are also expected to be fairly tolerant to fabrication errors. Our device exhibits simulated relative transmission efficiency and extinction ratio of 50% and 23dB, respectively, over an operating bandwidth of 40nm centered at $\lambda = 1.55\mu\text{m}$. The device was fabricated in a 300nm thick polysilicon (PolySi) layer defined on a silicon-dioxide under-cladding of thickness 3 μm . We chose this substrate due to our inability to obtain a conventional SOI wafer of the exact specifications and due to the fact that this substrate is similar to a conventional SOI wafer. Although we demonstrate a TE to TM polarization rotator, our method is readily adapted to TM to TE polarization rotators as well.

2. Design and simulations

As mentioned before, our design is based on a nonlinear search-based optimization, where the geometry of the device is chosen with fabrication constraints and the goal of maximizing a figure-of-merit (FOM). The FOM, for our device was the transmission efficiency of the TM polarization state assuming that the input was TE polarization. The device was comprised of a $5\mu\text{m} \times 1.2\mu\text{m}$ region of silicon that was discretized into 50×12 square pixels, each of size 100nm \times 100nm. The optimized geometry is illustrated in Fig. 1(a). The height of the pixels is same as the height of the input and output waveguides, which is the thickness of the top silicon layer (300 nm). This ensures that the entire device including the waveguides may be fabricated in a single lithography step. The optimization used a modified version of the direct-binary-search (DBS) algorithm, which has been described previously [39,40]. In designing this particular device, we chose a random initial layout of the 600 pixels and optimized their distribution using our modified DBS while maximizing the defined FOM. At each step, the electromagnetic fields within the device were calculated using MEEP, an open-source FDTD simulator developed at MIT, while the modified DBS algorithm was interfaced with this program using a Matlab front-end. In order to speed up the computation step, we used cloud based parallel computing on elastic computing servers hosted by Amazon Web Services. Each iteration of the optimization is completed once all pixels are toggled between their possible two states of existence: silicon and air. The total number of iteration steps was 50. The design took about 96 hours to be completed. The iterations terminate when the FOM does not improve beyond a predefined threshold. The steady state simulated light intensity distributions for the input TE and output TM polarization states are shown in Fig. 1(b) and Fig. 1(c), respectively. It is noted that coupled resonant modes are generated within the device (see [Visualization 1](#)) that interact in such a manner as to induce cross-coupling between the two polarization states, resulting in primarily TM mode in the output waveguide. For comparison with the NPR, we use a reference device, where the NPR is simply replaced by extending the input waveguide to the output port, as shown in the bottom inset in Fig. 1(d). Figure 1(d) shows the simulated transmission efficiency, which is defined as the ratio of the power in the TM polarization state at the output port to that in the TE polarization state at the output of the reference device. A peak efficiency of about 50% is obtained at $\lambda = 1.55\mu\text{m}$ for the NPR. The corresponding plot for the reference device confirms that no polarization rotation occurs when the NPR is absent. The operational bandwidth, where the transmission efficiency is within 2dB of the peak value, is 40 nm (1,528 nm to 1,568 nm).

Figure 1(e) shows the extinction ratio, which is defined as the ratio of the power in the TM polarization state to that in the TE polarization state, both measured at the output port. The simulations indicate that an extinction ratio of about 22.7dB at $\lambda = 1.55\mu\text{m}$ is achievable. Note that the FOM for our design was the transmission efficiency and not the extinction ratio.

Our simulations indicate two types of reflections from the device. Firstly, a fraction of the input TE light (~12.14%) is reflected after interacting with the nanopatterns. This reflected light couples out through the input port of the device. It is difficult to visualize this in both Fig. 1(b) and the supplementary animation movie since the input TE is much stronger.

Secondly, about 18.6% of the TM polarized light also couples to the input port as can be seen in Fig. 1(b) as well as the supplementary animation movie. Both contribute to the overall loss of the device. We attribute this issue to the fact that our optimization figure-of-merit (FOM) was only defined to maximize the transmission of the TM mode at the output port. The second loss could be decreased by simply imposing a condition to minimize the TM field coupling at the input waveguide port while maximizing it at the output waveguide. We would like to stress that due to the computational nature of our design, one may impose any condition in the FOM.

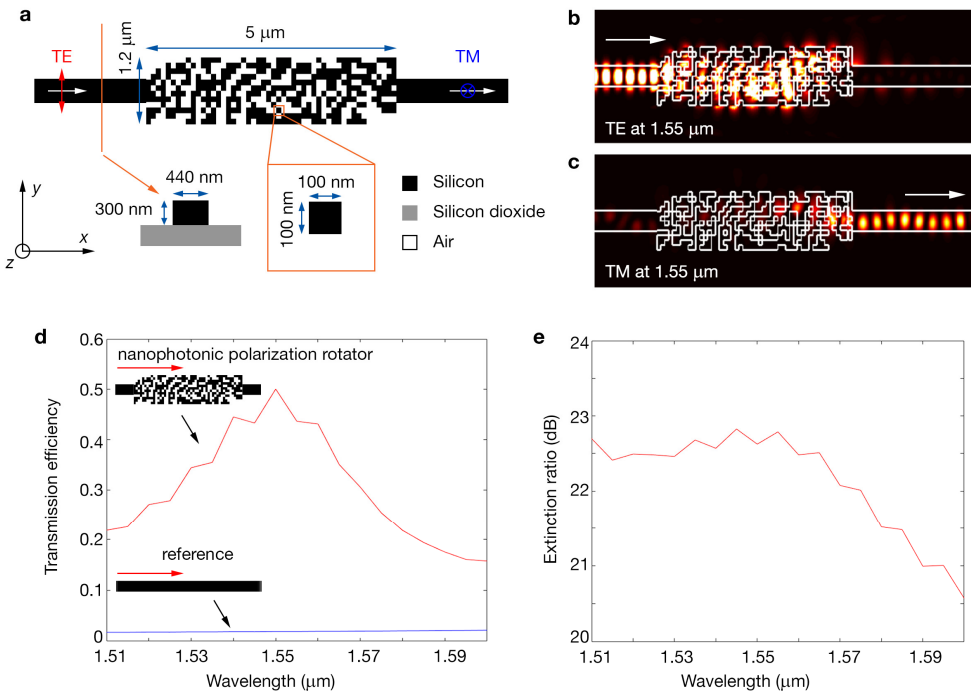


Fig. 1. The nanophotonic-polarization rotator (NPR). (a) Geometry of the NPR for rotating TE to TM. (b, c) Simulated steady-state intensity distributions for input TE polarized light (b) and output TM polarized light (c) at the design wavelength of $1.55\mu\text{m}$ (see [Visualization 1](#) for light propagation through the device). The white arrows in (a-c) show the direction of propagation of light through the device. TE is polarized in-plane and perpendicular to the direction of propagation, as illustrated by the red arrow in (a), while TM is polarized out-of-plane, as illustrated by the blue cross-in-circle in (a). (d) Simulated transmission efficiency of NPR (top) and reference device (bottom) as a function of wavelength. (e) Simulated extinction ratio as a function of wavelength.

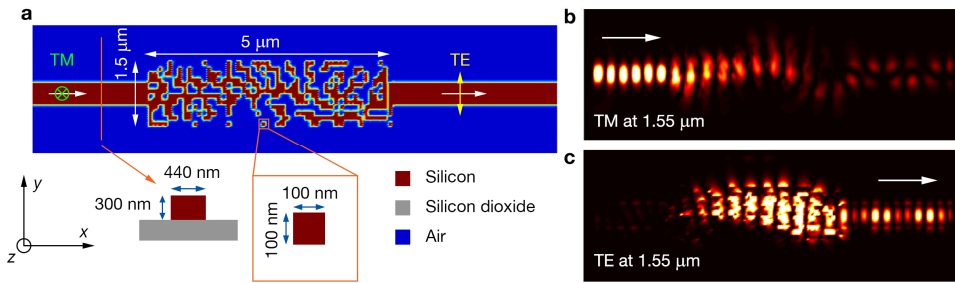


Fig. 2. A nanophotonic-polarization rotator (NPR) for rotating TM input to TE output. (a) Geometry of the NPR for rotating TM to TE. (b, c) Simulated steady-state intensity distributions for input TM polarized light (b) and output TE polarized light (c) at the design wavelength of $1.55\mu\text{m}$. The white arrows in (a-c) show the direction of propagation of light through the device. TE is polarized in-plane and perpendicular to the direction of propagation, as illustrated by the yellow arrow in (a), while TM is polarized out-of-plane, as illustrated by the green cross-in-circle in (a).

Our design method can be easily adapted to the reverse function, rotating TM polarization to TE polarization. A schematic showing the geometry of such a device is shown in Fig. 2(a). The simulated steady-state light distribution for input TM and output TE polarizations are shown in Fig. 2(b) and 2(c), respectively. The dimensions of this device are $5\mu\text{m} \times 1.5\mu\text{m}$ with individual pixel dimensions of $100\text{nm} \times 100\text{nm}$.

3. Fabrication

The TE to TM NPR from Fig. 1(a) was fabricated in a PolySi layer defined on top of a silicon under-cladding deposited on a single crystal silicon wafer. The thickness of the PolySi layer was 300 nm, and that of the oxide layer of $3\mu\text{m}$. The sample was prepared using the following procedure. A 4-inch single crystalline silicon wafer (University Wafers) was cleaned using acetone, methanol and isopropanol. Then, the wafer was etched using oxygen plasma to remove organic contaminants. Then, we deposited a $3\mu\text{m}$ thick silicon oxide (SiO_2) layer using plasma enhanced chemical vapor deposition (PECVD) to define the under-cladding. Lastly, we deposited polycrystalline silicon (PolySi) of thickness $\sim 300\text{nm}$. The layer thickness varied from 305 nm to 320 nm as measured using a Nanometrics Nanospec 3000 film analyser. PolySi also exhibits large granularity as shown in Fig. 3(a). Unfortunately, this also leads to undesired light scattering and contributes to losses in the device. The silicon deposition was carried out in an Expertech furnace using low power chemical vapor deposition (LPCVD) at 630°C and a deposition rate of $\sim 11.5\text{nm/min}$. A slot-waveguide based polarizer was also fabricated to control the input polarization state, the details of which are presented in Figs. 3(b) - 3(e). The polarizer is essentially a single-mode waveguide with a $10\mu\text{m}$ air-slot that is 70 nm offset from the center of the waveguide as shown in Fig. 3(b). The polarizer allows only the passage of TM polarization as shown in the simulated steady state light field patterns in Fig. 3(d) and 3(e). A scanning electron micrograph of the fabricated polarizer is shown in Fig. 3(c).

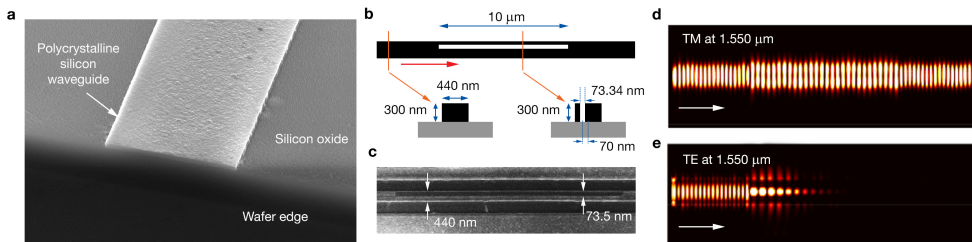


Fig. 3. (a) Scanning electron micrograph of the wafer edge showing granularity in the PolySi waveguide. (b) Diagrammatic representation of the on-chip polarizer, which is a single mode silicon (black) waveguide (440nm wide) with a 10 μm long horizontal air slot (white) having a 70nm offset to the center of the waveguide. The polarizer is fabricated in the top 300nm PolySi layer. The red arrow denotes the direction of light travel through the polarizer. (c) Scanning electron micrograph of the on-chip polarizer used in the experiments. (d, e) Simulation showing steady state light field patterns for TM and TE mode in the on-chip polarizer, respectively.

Our NPR and the waveguides can be patterned using a single lithography step. However, we did not have access to tools with sufficient resolution and field size. Therefore, we opted for a two-step process, where the large features were fabricated using optical lithography, and the fine features were created using focused-ion-beam patterning. The top most PolySi layer was first cleaned using acetone, methanol, isopropanol and subsequent oxygen plasma etching. Then a thin layer of Hexamethyldisilazane (HMDS) was spun on top of the layer as an adhesion promoter. The sample was then coated with a ~500nm thick layer of Shipley S1805 photoresist. Photolithography was carried out using the direct laser writing (DLW) optical lithography tool Heidelberg μ PG 101 to pattern all multimode waveguides and tapers. The photoresist was then developed by immersing the sample in AZ 1:1 developer for 60 seconds, followed by rinsing in DI water for 60 seconds to clean the sample of residual developer. The patterned photoresist layer was then used as a mask to etch the top silicon layer using an Oxford 100 etcher with a modified Bosch process. We used a 3 second etch step of SF₆ gas flowing at 40sccm and C₄F₈ gas flowing at 17.5sccm, followed by an immediate 2 second passivation step of only C₄F₈ gas flowing at 17.5sccm, while operating the chamber at 0°C. This gave us an effective silicon etch rate of ~10 nm/min.

In the second step, focused-ion beam (FiB) patterning using a FEI Helios NanoLab 650 was used to define the NPR and the single-mode waveguides. The beam current used was 7.7 pA with a fluence of 800 C/m². Standard alignment marks and fiducials were used to align the patterns between the optical lithography and the FiB patterning steps and to correct for systematic beam drift caused by charging effects and change of surrounding temperature. We also fabricated reference devices (without the NPR) on the same wafer for data normalization. A scanning-electron micrograph of the fabricated NPR is shown in Fig. 4(a).

4. Device characterization

The device was characterized using an optical set-up described in our previous work [32–36]. The setup used to characterize the fabricated NPR device is schematically shown in Fig. 4(b). Standard single-mode lensed fibers were used at the input and output to couple light from and into the multimode waveguides that then taper down to the corresponding single-mode waveguides. The source was a Hewlett-Packard 8186F tunable laser source emitting in the range 1.508 μm to 1.640 μm .

First, the single-mode lensed fiber at the input was aligned to the on-chip polarizer. Edge-coupling was used to couple light from the lensed fiber to the waveguide that delivers light to the on-chip polarizer. The output was also collected using a single-mode lensed fiber. At first, the optical components in the dotted box were bypassed by connecting the output lensed fiber directly to the detector. The fiber polarization controller PC1 was adjusted to set the input polarization state to TE by monitoring the power at the detector. The on-chip polarizer only

allows the TM mode to pass through efficiently while blocking the TE mode as shown in Fig. 3(d) and 3(e). Hence, we set the input polarization to be TE mode by minimizing the power received at the detector. Next, the input lensed fiber was moved to probe the reference device. The optical components in the dotted frame were inserted in the path. The fiber polarization controller PC2 was then adjusted to align the polarization plane of the output light with that of the polarizer in between the two collimators. Once aligned, the polarizer was rotated to select either the TE or the TM components at the output. Lastly, the input lensed fiber was moved to probe the NPR. TE polarized input was coupled into the NPR and the power and polarization state of the output light were measured. The same measurements were also conducted with the reference device. As described earlier, the transmission efficiency was computed relative to the reference device to account for any inadvertent polarization rotation that occurs during the free-space-to-waveguide coupling and during the taper from multi-mode to single-mode waveguides.

We plotted the transmission efficiency as a function of wavelength in Fig. 4(c) for both the NPR and the reference device. The measurements indicate a peak transmission efficiency of 37% at $\lambda = 1.55\mu\text{m}$. The output TM power in the reference device was low as expected. The extinction ratio as a function of wavelength is plotted in Fig. 4(d), and shows a peak value of 9dB at $\lambda = 1.55\mu\text{m}$. In comparison, the simulated values were 50% and 23dB, respectively. We attribute these differences to two reasons. First, polysilicon that we used for the device layer contributes to light scattering and increased losses due to its granularity and non-uniformity. Also, grain boundaries in polySi may lead to the presence of unbound electrons that may contribute to added scattering losses. Other sources of losses include electronic absorption, unwanted tunneling, absorption within a grain, etc [41]. Second, there may be the possibility of Ga contamination to the device from the FiB step. Although it is difficult for us to quantify this, it is a well investigated issue as reported in Ref. 42. Lastly, fabrication errors due to the limitations of our current process inevitably lead to some loss in performance. In order to illustrate their impact, we simulated the normalized transmission efficiency and extinction ratio at $\lambda = 1.55\mu\text{m}$ as a function of these errors. The normalization was done with respect to maximum transmission at $\lambda = 1.55\mu\text{m}$ when there is no fabrication error.

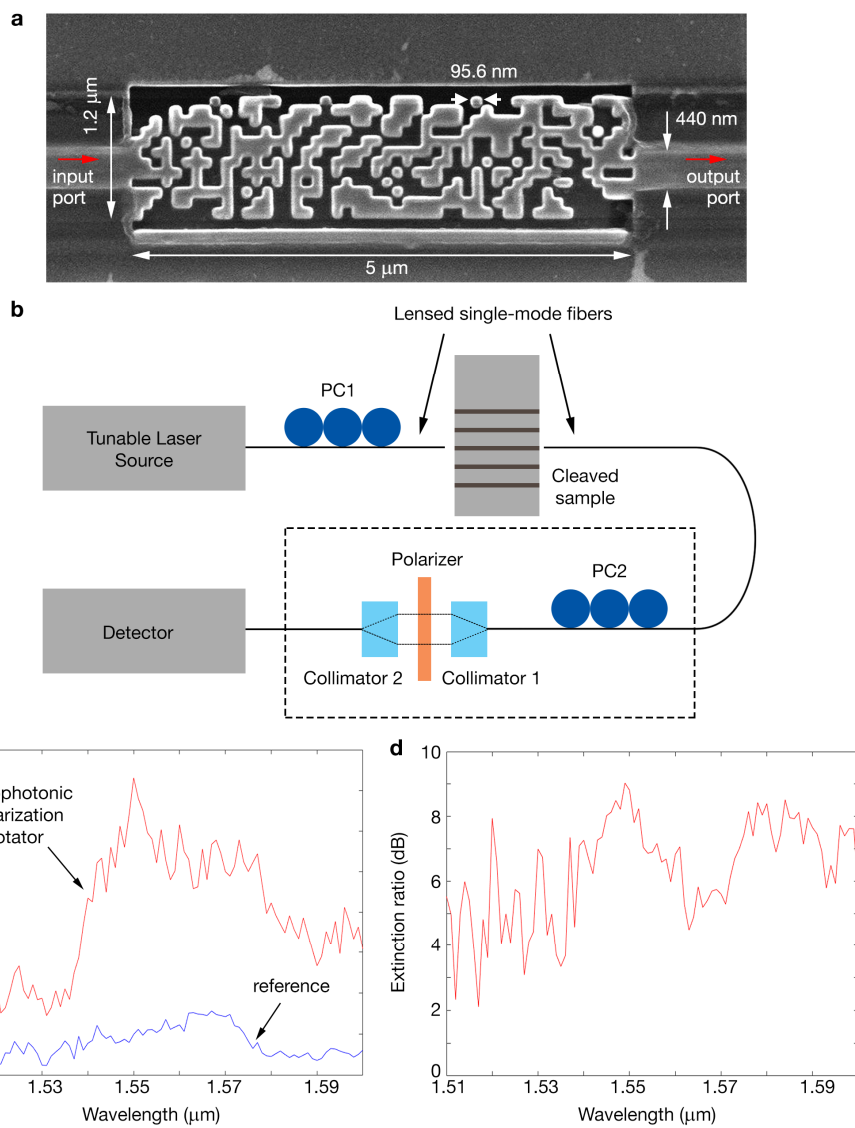


Fig. 4. Characterization of the NPR. (a) Scanning-electron micrograph of the fabricated NPR. The red arrows indicate the direction of propagation of light through the device. (b) Schematic of the measurement setup used to characterize the NPR. The input and output fibers are standard single-mode lensed fibers. PC1 and PC2 are fiber polarization controllers. The polarizer is used to select either the TE or TM component of the output. Measured (c) relative transmission efficiency and (d) extinction ratio of TM output with TE input. The transmission efficiency is plotted relative to the reference device as described in the text.

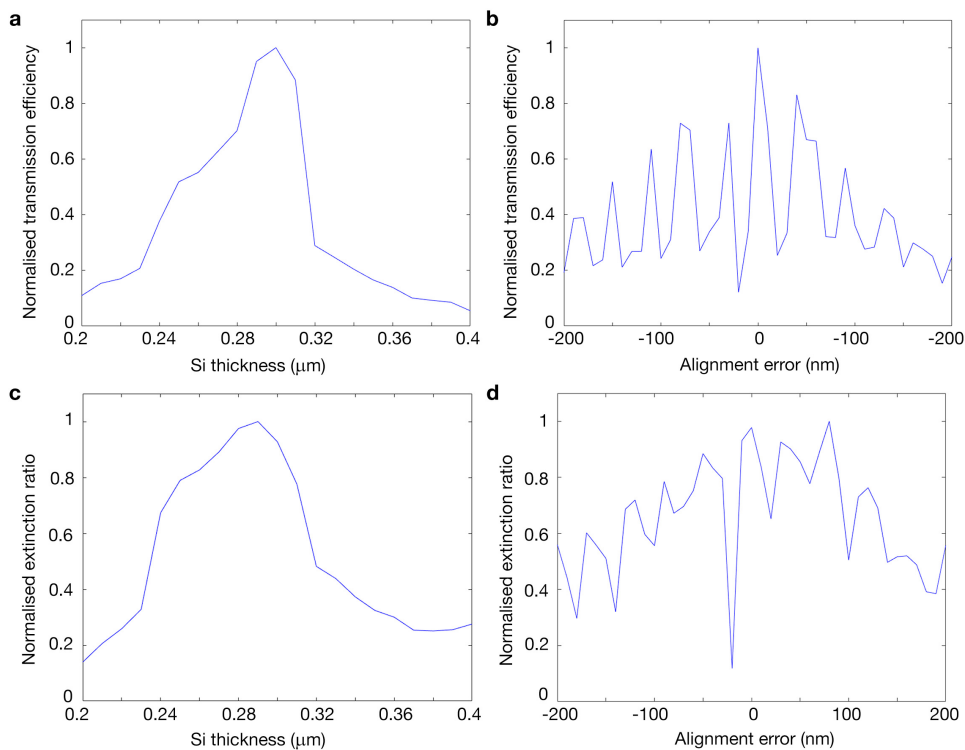


Fig. 5. Effect of fabrication errors. (a) Simulated normalized relative transmission efficiency and (c) simulated extinction ratio at $\lambda = 1.55\mu\text{m}$ as a function of errors in the silicon-layer thickness. The same metrics as a function of misalignment between input and output waveguides and the NPR are shown in (b) and (d), respectively.

Figures 5(a) and 5(c) show the effect of varying the thickness of the silicon layer. The height of the pixels (Si layer thickness) was uniformly varied from 200nm to 400nm, and the performance of the resulting device was computed. A 10nm variation in this thickness causes 11% and 23% decrease in the transmission efficiency and extinction ratio, respectively. Figures 5(b) and 5(d) show the impact of misalignment between the input/output waveguides and the NPR. Unfortunately, the NPR seems to be sensitive to this alignment, and we believe this contributed significantly to the discrepancy between experiment and simulation for our fabricated device. It is important to note that this error can be solved readily by using a single-step lithography process that avoids any alignment steps.

We also note that it is possible to increase the robustness of these devices by incorporating a robustness criterion to the FOM during design, similar to a previous diffractive device that we have demonstrated before [43].

5. Conclusions

In summary, we designed, fabricated and characterized an ultra-compact nanophotonic polarization rotator. The compact footprint is achieved due to the application of numerical optimization on what we refer to as a digital metamaterials device. Our simulations indicate transmission efficiency of 50% and extinction ratio of 22.65dB and an operating bandwidth of 40nm. We were able to experimentally show transmission efficiency of 37% and extinction ratio of 9dB, which were limited by the constraints of our fabrication process. Nevertheless, our device can be CMOS compatible for large-scale integration. Finally, we emphasize that our methodology is general and we simulated a TM to TE NPR as well. Photonic functions

can be encoded as subwavelength pixel distributions that are computationally optimized and we refer to these devices as digital metamaterials.

Funding

University of Utah USTAR shared facilities, MRSEC Program of the National Science Foundation (NSF, DMR-1121252)

Acknowledgments

The authors thank S. Pritchett, B. Baker and A. Banerjee for assistance with the fabrication. This work made use of the University of Utah shared facilities of the Micron Technology Foundation Inc. Microscopy Suite sponsored by the College of Engineering, Health Sciences Center, Office of the Vice President for Research and the Utah Science Technology and Research (USTAR) initiative of the State of Utah.